Applied Science and Engineering Progress, Vol. 20, No. 3, 2027, 8288

Research Article

Comparative Study on the Microstructure, Hardness, and Corrosion Behavior of CoCrFeNi Alloy and CoCrFeNiCu High Entropy Alloy Cladded Layers on SS304 Substrate Fabricated by GTAW

Pongpak Chiyasak, Thanawat Santawee, Surapit Posri, and Aphichart Rodchanarowan*
Department of Materials Engineering, Faculty of Engineering, Kasetsart University, Chatuchak, Bangkok, Thailand

* Corresponding author. E-mail: fengacrw@ku.ac.th DOI: 10.14416/j.asep.2026.09.002
Received: 20 May 2026; Revised: 10 July 2026; Accepted: 13 July 2026; Published online: 1 September 2026

Abstract
In this study, equiatomic CoCrFeNi alloy and CoCrFeNiCu high entropy alloy (HEA) cladded layers were fabricated on SS304 substrates using gas tungsten arc welding (GTAW). The microstructure, phase composition, hardness, and corrosion behavior of cladded layers were systematically investigated. The microstructure of the CoCrFeNi alloy cladded layer was homogeneous with a single FCC phase, while the CoCrFeNiCu HEA cladded layer exhibited a heterogeneous microstructure due to Cu segregation. Cu addition increased the hardness of the cladded layer from 126.6 ± 2.8 HV for the CoCrFeNi alloy system to 163.9 ± 2.2 HV for the CoCrFeNiCu HEA system. Electrochemical characterization in the 3.5 wt% NaCl solution showed that the CoCrFeNi alloy cladded layer had better corrosion resistance, with lower corrosion current density (6.92 $\mu A/cm^2$), higher corrosion potential (-492 mV vs. SCE), and higher oxide film resistance (12.48 $k\Omega \cdot cm^2$), compared to the CoCrFeNiCu HEA cladded layer (19.50 $\mu A/cm^2$, -621 mV vs. SCE, and 0.51 $k\Omega \cdot cm^2$, respectively). The improved corrosion resistance of the CoCrFeNi alloy was attributed to the formation of a more stable and homogeneous passive oxide film. In contrast, Cu segregation led to compositional heterogeneity, resulting in selective corrosion through microgalvanic coupling. Overall, Cu addition enhanced the hardness but reduced the corrosion resistance, demonstrating a tradeoff between the mechanical and electrochemical performance of GTAW-fabricated HEA cladded layers. These findings demonstrate the potential of compositional design for tailoring the properties of HEA-clad layers for advanced surface engineering applications.

Keywords: Corrosion, Gas Tungsten Arc Welding, Hardness, High Entropy Alloys

1 Introduction

High entropy alloys (HEAs) are a new class of advanced metallic materials that have five or more principal elements in near equiatomic proportions. Unlike conventional alloys, which are typically formulated with one principal element, HEAs possess high configurational entropy that favors the formation of simple solid solution phases instead of complex intermetallic compounds. Yeh *et al*., [1] introduced the idea of high configurational entropy for the design of multicomponent alloys. Cantor *et al*., [2] showed the formation of a stable FCC solid solution in equiatomic multicomponent alloys. These novel investigations have resulted in extensive reports on HEAs possessing an excellent combination of mechanical strength, corrosion resistance, thermal stability, and wear resistance due to the synergistic effects of high configurational entropy, sluggish diffusion, lattice distortion, and cocktail effect [3]. Thus, HEAs have attracted considerable attention for advanced structural and surface engineering applications.

The CoCrFeNi alloy is considered a standard face-centered cubic (FCC) alloy in many alloy systems, owing to its excellent phase stability and corrosion resistance. The previous literature reported that equiatomic CoCrFeNi has a stable single-phase FCC structure with a homogeneous microstructure, making it an ideal base alloy for compositional modification [4]. It has been observed that the superior corrosion resistance of CoCrFeNi alloys is mainly attributed to the formation of a stable Cr rich passive oxide film [5]. The addition of V,

Applied Science and Engineering Progress, Vol. 20, No. 3, 2027, 8288

Nb, and Ta has been reported to improve the mechanical performance of CoCrFeNi-based alloys through severe lattice distortion and solid solution strengthening [6]. Later, other studies extended this alloy design strategy by incorporating Cu and Ti into the CoCrFeNi alloy system, demonstrating that these additions effectively modify the microstructure and improve hardness [7]. Among these alloying elements, Cu has attracted particular attention because of its low cost and strengthening effect in CoCrFeNi-based HEAs [8]. However, the positive ΔH_{mix} between Cu and the other constituent elements leads to elemental segregation during solidification [9]. The resulting Cu induced compositional heterogeneity improves hardness but may also contribute to reduced passive film stability, resulting in lower corrosion resistance [8]-[10]. Therefore, Cu addition results in a compromise between mechanical properties and corrosion resistance, which leads to the need for further research on the Cu containing CoCrFeNi HEA cladded layers.

Surface engineering has been systematically used to enhance the surface performance of structural materials, while preserving the desirable mechanical properties of the substrate [11]. Different cladding techniques such as laser cladding [12], plasma cladding [13] and Laser Engineered Net Shaping (LENS) [14] have been successfully used to produce HEA coatings with improved wear and corrosion resistance. Laser cladding can produce dense layered coatings with low dilution and fine microstructures [12]. Plasma cladding can be used for surface modification of large areas with high deposition efficiency [13]. LENS, on the other hand, provides good control of composition, but the processing is relatively complicated and the equipment cost is high [14]. The fusion-based cladding processes [11] depend on the controlled heat input and rapid solidification to achieve stable metallurgical bonding. The processing parameters strongly influence the thermal characteristics, dilution, and resulting microstructure during fusion-based surface processing [15], [16]. Among these techniques, gas tungsten arc welding (GTAW) is an attractive technique for industrial surface engineering applications due to its stable electric arc, excellent metallurgical bonding, and relatively low processing cost.

The design of the alloy plays a significant role in controlling the microstructure and properties of HEA cladded layers fabricated by GTAW, as evidenced by previous studies. The effects of Sn and Ti additions on the microstructure, phase composition, hardness, and corrosion behavior of CoCrFeNi-based HEA cladded layers have been investigated, demonstrating that alloying additions significantly modify these properties [17]. Moreover, the subsequent studies have shown that the alloy composition modification can change the phase composition and mechanical performance of the GTAW-fabricated HEA cladded layers [18]. Also, other studies highlighted that the solidification behavior during GTAW processing influences the elemental distribution, microstructural evolution, and corresponding corrosion performance of HEA cladded layers [19], [20]. These studies demonstrate that both alloy composition and solidification features are important factors in controlling the properties of GTAW-fabricated HEA cladded layers. However, prior studies mostly concentrated on single alloying elements or individual properties, while a systematic comparison between the equiatomic CoCrFeNi alloy and CoCrFeNiCu HEA cladded layers is very limited. In particular, the effect of Cu segregation on the relationships between phase formation, microstructural evolution, hardness, and electrochemical corrosion behavior in GTAW fabricated cladded layers has not been fully clarified. Recent bibliometric analyses have also highlighted the growing research interest in advanced welding technologies, emphasizing the need for continued investigations into the relationships between processing, microstructure, and material properties [21].

In this work, equiatomic CoCrFeNi alloy and CoCrFeNiCu HEA cladded layers were fabricated on SS304 substrates using the GTAW cladding technique. Prior to cladding, the HEA powders were prepared by mechanical alloying to promote homogeneous elemental distribution. The fabricated cladded layers were systematically characterized in terms of phase constitution, microstructure, elemental distribution, hardness, and electrochemical corrosion behavior. The impact of Cu addition on the properties of the CoCrFeNi alloy and CoCrFeNiCu HEA cladded layers was systematically investigated.

2 Materials and Methods

2.1 *Raw materials*

The cladding experiments were performed on SS304 substrates of 50 mm × 50 mm × 12 mm. The surface preparation prior to deposition was performed by mechanical polishing and cleaning to remove contaminants. Metal powders (Co/Cr/Fe/Ni/Cu) with 99% purity and particle size less than 44 μm (-325 mesh) were employed as starting materials for the

fabrication of the HEA cladded layers. Metal powders were weighed as an equiatomic composition to produce an equiatomic CoCrFeNi alloy and CoCrFeNiCu HEA cladded layers. Subsequently, the weighed metal powder was milled by a high speed ball mill (Fritsch, Pulverisette 6, Germany) with a ceramic Al_2O_3 vial in an Ar atmosphere to ensure a homogeneous elemental distribution. The milling process was performed at 300 rpm for 20 h with a ball-to-powder weight ratio of 10:1. The milled metal powders were then loaded into a metal mold of dimensions 30 mm × 5 mm × 3 mm and were compacted into a metallic rod using a hydraulic pressing machine at a pressure of 100 MPa.

2.2 *Cladding process*

Figure 1 illustrates the experimental schematic of the GTAW process used for the fabrication of CoCrFeNi alloy and CoCrFeNiCu HEA cladded layers. During cladding, the high temperature generated by the electric arc melted the metal rods and formed HEA cladded layers on the substrate surface. The cladding was performed by a single pass bead on plate to obtain a single layer cladded on the SS304 substrate. After cladding, the samples were cooled in air to room temperature. Table 1 presents the GTAW processing parameters for the fabrication of equiatomic CoCrFeNi alloy and CoCrFeNiCu HEA cladded layers on SS304 substrates.

Table 1: GTAW processing parameters used for fabrication of equiatomic CoCrFeNi alloy and CoCrFeNiCu HEA cladded layers on SS304 substrates.

Processing condition	Value
Arc current	130 A
Cladding speed	35 cm/min
Shielding gas	Argon, 20 L/min
Electrode specification	Thoriated electrode

2.3 *Characterizations*

Cladded samples were cut with a high speed cutting machine. Samples were ground progressively with abrasive papers of 320, 600, 800, 1200, and 2000 grit sizes and polished with 0.1 µm diamond suspension. The prepared surfaces were subsequently etched in aqua regia solution for 15 s. The microstructure and chemical compositions of the cladded layers were investigated by a scanning electron microscope (SEM, Hitachi SU3500) equipped with energy dispersive spectroscopy (EDS).

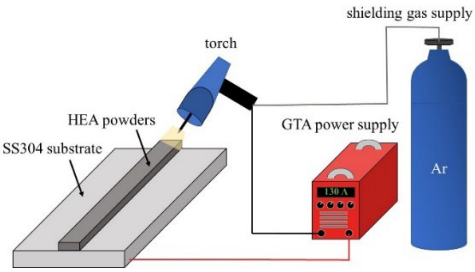

Figure 1: Experimental schematic of the GTAW process employed for fabrication of CoCrFeNi alloy and CoCrFeNiCu HEA cladded layers.

The phase composition was identified by X-ray diffraction (XRD, PANalytical Empyrean) with Cu Kα radiation in the 2θ range from 20° to 90°. The Vickers hardness was measured by a Vickers microhardness tester (Mitutoyo, MVK-H1) at a load of 500 gf and a dwell time of 15 s. The areas of the hardness indentations, including cladded layer, heat-affected zone (HAZ), and substrate regions, and the position of indents are depicted in Figure 2. Each region was indented ten times, and the hardness was reported as the Vickers average hardness (mean ± standard deviation (SD)) in the HV scale. Statistical analysis of the hardness measurement was performed using analysis of variance (ANOVA), followed by Fisher's least significant difference (LSD) post hoc test, in OriginPro 8 software. Differences were considered statistically significant at p-value < 0.05.

Corrosion behavior and passive film stability of the cladded layers were evaluated by electrochemical corrosion investigations in linear polarization and Electrochemical Impedance Spectroscopy (EIS) modes using a potentiostat/galvanostat (PalmSens, PalmSens4).

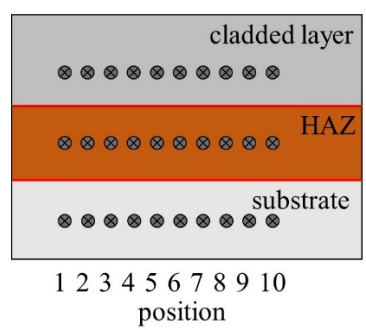

Figure 2: Hardness indentation positions used for Vickers hardness measurements in the cladded layer, HAZ, and substrate (ten indents per area).

Applied Science and Engineering Progress, Vol. 20, No. 3, 2027, 8288

The corrosion potential (E_{corr}) and corrosion current density (i_{corr}) were obtained by fitting the anodic and cathodic slopes using the PSTrace 5.9 software. The pitting potential (E_{pitt}) was defined as the potential at where a rapid increase in anodic current density was observed. The measurements were carried out at room temperature in a standard three-electrode electrochemical cell containing 3.5 wt% NaCl solution using a platinum wire as counter electrode, a saturated calomel electrode (SCE) as reference electrode, and the samples as working electrode. Each sample surface area was approximately 0.25 cm^2. The corrosion-related parameters were obtained by analyzing the linear polarization curve at a sweep rate of 0.01 V/s and the potential range from -2 to 2 V vs. SCE. The polarization scan was performed over a sufficiently wide potential range to determine the E_{corr}, i_{corr}, and E_{pitt} while capturing the passive behavior of the cladded layers. EIS was performed in the frequency range of 100 kHz to 0.1 Hz with the AC signal amplitude of 10 mV. The electrochemical impedance-related parameters were calculated, and the EIS spectra were analyzed by PSTrace 5.9 software by fitting to an equivalent electrical circuit (EEC) model. The equivalent circuit model of $R_s{\cdot}[R_{oxide}CPE_{oxide}]$ was chosen as the impedance spectra showed a single capacitive semicircle [22]. The electrochemical parameters were obtained by fitting the experimental impedance spectra with a nonlinear least squares fitting procedure performed in PSTrace 5.9 software.

3 Results and Discussion

3.1 *HEA parameters*

The phase structure of HEAs can be predicted based on thermodynamic and atomic parameters, including a mixing entropy (ΔS_{mix}), mixing enthalpy (ΔH_{mix}), atomic size difference (δ), electronegativity difference ($\Delta\chi$), and valence electron concentration (VEC), which have been reported in previous literature [23], [24]. Equations (1) - (5) were used to determine these five parameters. The variables used in the equations consist of the gas constant (R), atomic fraction (c_i), mixing enthalpy between unlike atomic pairs (Ω_{ij}), atomic radius (r_i), Pauling electronegativity (χ_i), and valence electron concentration (VEC_i).

$$\Delta S_{mix} = -R\sum c_i ln c_i \quad (1)$$

$$\Delta H_{mix} = \sum_{i=1\, i\neq j}^{n} c_i c_j \Omega_{ij} \quad (2)$$

$$\delta = 100^{*}\sqrt{\sum_{i=1}^{n} c_i \left(1-\frac{r_i}{\bar{r}}\right)^2} \quad (3)$$

$$\Delta\chi = \sqrt{\sum_{i=1}^{n} c_i(\chi-\bar{\chi})^2} \quad (4)$$

$$VEC = \sum_{i=1}^{n} c_i{}^{*}(VEC)_i \quad (5)$$

The mixing enthalpy between unlike atomic pairs is taken from the literature [25]. The atomic radius, Pauling electronegativity, and VEC of each element are obtained the standard reference data [26]. The calculated thermodynamic and atomic parameters of the CoCrFeNi alloy and CoCrFeNiCu HEA cladded layers are listed in Table 2.

According to the reported phase formation criteria, HEAs tend to form an FCC solid solution structure when the alloy system exhibits the ΔH_{mix} within the ranges of -11.6 to 3.2 kJ/mol, δ values below 6.6%, and VEC values above 8, respectively [27], [28]. However, the positive ΔH_{mix} (3.05 kJ/mol) and larger δ (1.01%) reported in the CoCrFeNiCu HEA system could result in partial phase separation or compositional heterogeneity. Although both alloys are expected to form a single FCC solid solution structure, the CoCrFeNi alloy system is predicted to generate a more stable and homogeneous phase, while the CoCrFeNiCu system has a less uniform microstructure with a tendency for segregation [29].

Table 2: Calculated HEA characteristic parameters used to predict phase formation of the CoCrFeNi alloy and CoCrFeNiCu HEA cladded layers.

Alloys	ΔH_{mix} (kJ/mol)	ΔS_{mix} (J/molK)	δ (%)	$\Delta\chi$	VEC
CoCrFeNi	-3.76	11.52	0.30	0.09	8.23
CoCrFeNiCu	3.05	13.38	1.01	0.09	8.76

3.2 *Microstructure, chemical composition, and elemental distribution*

Figure 3 shows the cross sectional SEM images of the CoCrFeNi alloy and CoCrFeNiCu HEA samples. In both alloy systems, three distinct zones, the cladded layer, the heat-affected zone (HAZ), and the substrate,

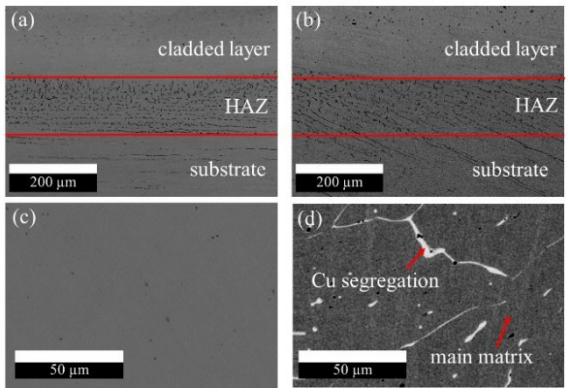

Figure 3: Cross sectional SEM images of (a) CoCrFeNi alloy and (b) CoCrFeNiCu HEA systems including cladded layer, HAZ, and substrate, (c) CoCrFeNi alloy cladded layers, and (d) CoCrFeNiCu HEA cladded layers at higher magnification.

are clearly identified. The upper region is the deposited HEA cladded layer. The HAZ is the middle area where the substrate was thermally affected during the GTAW process, but not completely melted.

The thermal cycle during the cladding process determines the formation of the HAZ and the degree of microstructural modification in the substrate. A similar behavior was observed for laser-based manufacturing processes, where the heat input has a strong influence on the HAZ characteristics and the microstructural evolution [30]. The lower region corresponds to the unaffected SS304 substrate that retained its original microstructure. The distinct boundary between the cladded layer, HAZ, and the substrate indicates that the GTAW process parameters selected led to a well defined cladded layer with minimal thermal effect on the substrate.

Moreover, no interfacial cracks, pores, or delamination were observed at the boundary of the cladding, suggesting strong metallurgical bonding after the cladding process. The continuous bonded interface indicates that the cladded alloy and substrate were completely merged during the GTAW processing, and hence, a good interfacial integrity was achieved. Similar interfacial features were observed in welded and surface-engineered alloys where strong metallurgical bonding is necessary to provide the integrity of the interface and the reliability of the structure [31].

The SEM images at higher magnification reveal differences in solidification morphologies in the two cladded layers. Figure 3(c) shows the microstructure of the CoCrFeNi alloy cladded layer, which is relatively homogeneous and has no visible secondary phase. In contrast, the CoCrFeNiCu HEA cladded layer (Figure 3(d)) exhibits a heterogeneous microstructure of dendrites (gray) and interdendrites (bright). The welding thermal cycle has a significant effect on the observed microstructure. As reported in previous studies, the thermal cycle controls phase transformation and microstructural evolution, leading to heterogeneous microstructure under different thermal conditions [32], [33]. The heterogeneous microstructure observed in the present work is associated with the Cu addition. The limited solubility of Cu and its positive mixing enthalpy of unlike atom pairs with the other constituent elements promote elemental segregation during solidification [9]. The bright interdendritic regions are formed due to elemental segregation during solidification. The positive mixing enthalpy of unlike atom pairs between Cu and other constituent elements results in the segregation of Cu in the interdendritic regions, while Co, Cr, Fe, and Ni are retained in the dendritic matrix [9]. In addition to the thermodynamic driving force, the rapid cooling associated with the GTAW process limits long range elemental diffusion, thereby retaining the heterogeneous microstructure formed during solidification [17], [32].

The EDS mapping results of the CoCrFeNi alloy and CoCrFeNiCu HEA cladded layers are shown in Figure 4(a) and (b), respectively. These results further confirm the elemental distributions and support the proposed interpretation of the solidification behavior. The CoCrFeNi alloy cladded layer shows a more uniform distribution of Co, Cr, Fe, and Ni in the investigated region, with good elemental homogeneity after GTAW processing. No significant elemental enrichment or depletion is detected. This indicates that the constituent elements were homogeneously distributed in the FCC matrix. Similar homogeneous elemental distributions have also been reported in CoCrFeNi-based HEAs with stable single phase solid solution structures [5]. In contrast, the element distribution of the CoCrFeNiCu HEA cladded layer exhibits a heterogeneous microstructure with Cu segregation distributed throughout the matrix of the CoCrFeNi-based HEA. The Cu addition is linked with the observed depletion of Co, Cr, Fe, and Ni, suggesting that elemental segregation takes place during solidification. This heterogeneous elemental distribution is in agreement with the microstructure demonstrated in the SEM images (Figure 3(d)), where the bright interdendritic regions correspond to the Cu segregation.

Applied Science and Engineering Progress, Vol. 20, No. 3, 2027, 8288

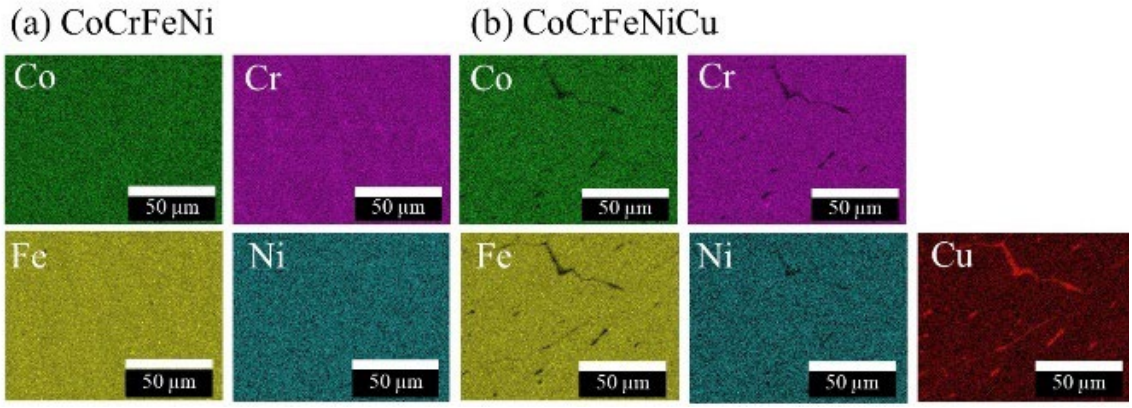

Figure 4: Elemental distribution of (a) CoCrFeNi alloy and (b) CoCrFeNiCu HEA cladded layers obtained from EDS mappings.

The thermodynamic characteristics of the HEA system provide an explanation for the observed segregation behavior. In general, stable solid solution formation is preferred when the mixing enthalpy values of unlike pairs are low or negative, such as Cr-Ni (-7 kJ/mol), Fe-Ni (-2 kJ/mol), and Co-Fe (-1 kJ/mol). On the other hand, Cu shows positive mixing enthalpy with some constituent elements such as Cu-Co (6 kJ/mol), Cu-Cr (12 kJ/mol), and Cu-Fe (13 kJ/mol). These positive values suggest limited solubility between Cu and other constituent elements and, therefore, favor elemental segregation during solidification. Cu preferentially segregates in the interdendritic regions instead of being homogeneously incorporated in the FCC matrix [25]. Also, the fast solidification in GTAW limits the long range diffusion of elements and consequently retains compositional heterogeneity after solidification [17], [32].

The chemical composition obtained by EDS analysis is given in Table 3. Results indicate that the chemical compositions of both CoCrFeNi alloy and CoCrFeNiCu HEA cladded layers are close to the designed equiatomic ratios. Although Cu segregation was observed in the CoCrFeNiCu HEA cladded layer (Figure 3(d)), the overall chemical composition shows no significant elemental loss during the GTAW process. The chosen GTAW processing conditions were able to retain the nominal alloy composition, despite the relatively low melting temperature of Cu [34].

Table 3: Chemical compositions of the CoCrFeNi alloy and CoCrFeNiCu HEA cladded layers obtained from EDS mapping measurements.

Alloys	Chemical composition (at.%)				
	Co	Cr	Fe	Ni	Cu
CoCrFeNi	24.82	25.37	25.11	24.70	-
CoCrFeNiCu	20.87	20.34	20.12	19.76	18.91

Figure 5 shows the EDS linescan analyses of the CoCrFeNi alloy and CoCrFeNiCu HEA cladded layers. The analyses were conducted at a higher magnification to more clearly reveal the elemental distributions. The intensity profiles of Co, Cr, Fe and Ni were almost constant along the whole scanning path for the CoCrFeNi alloy cladded layer, which indicated homogeneous distribution of elements without visible segregation of elements. This observation is in agreement with the uniform microstructure observed in the SEM image (Figure 3(c)) and supports the formation of a homogeneous single FCC solid solution [5], [35].

In contrast, the elemental distributions of the CoCrFeNiCu HEA cladded layer reveal significant differences. The intensity of Cu increased significantly in the bright interdendritic regions, while the intensities of Co, Cr, Fe, and Ni decreased at the same time. The corresponding variation confirms the elemental segregation and the presence of Cu segregation during solidification. This segregation behavior is caused by the positive mixing enthalpy of unlike atom pairs between Cu and the other elements, which lowers solubility and causes Cu enrichment in the interdendritic regions [25], [36]. Moreover, the rapid solidification associated with the GTAW process limits the long range diffusion of elements,

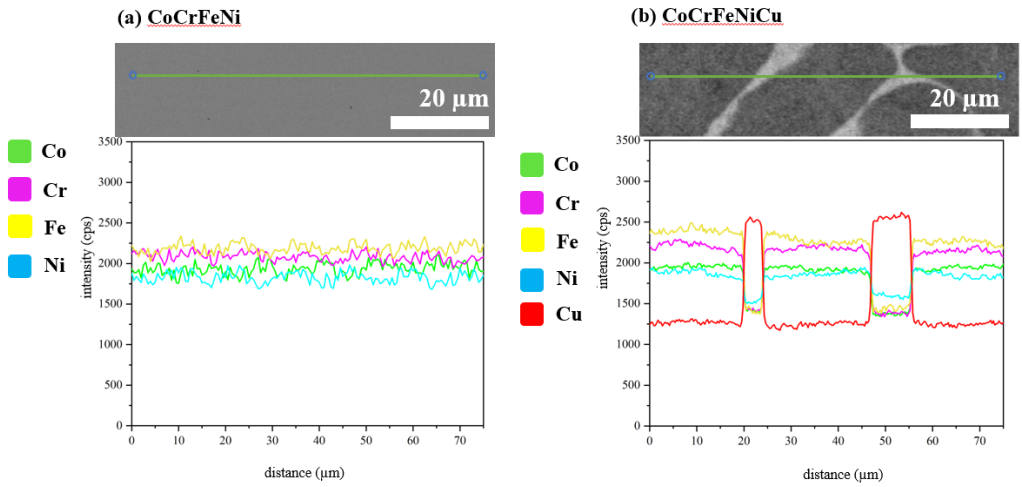

Figure 5: EDS linescan profile of (a) CoCrFeNi alloy and (b) CoCrFeNiCu HEA cladded layers obtained along the selected scanning paths.

maintaining compositional heterogeneity after solidification [17].

The EDS linescan results provide direct evidence to support the microstructure in the SEM images (Figure 3) and elemental mapping results (Figure 4). The segregation of Cu in the interdendritic regions with depletion of Co, Cr, Fe, and Ni indicates that Cu addition has a significant impact on elemental distribution in the CoCrFeNi matrix. The compositional heterogeneity is expected to increase the lattice distortion and result in the higher hardness of the CoCrFeNiCu HEA cladded layer [7], [37].

3.3 *Phase analysis by XRD*

Figure 6(a) shows the XRD pattern of the CoCrFeNi alloy and CoCrFeNiCu HEA cladded layers. The CoCrFeNi alloy cladded layer exhibits (111), (200), and (220) diffraction peaks at 43.96, 51.21, and 75.36°, respectively. The diffraction peaks are consistent with the single FCC phase of the CoCrFeNi system provided by the reference card (ICDD:04-018-7506). However, the CoCrFeNiCu HEA cladded layer shows the diffraction peaks of (111), (200), and (220) at 43.89°, 51.07° and 75.12°, respectively. The diffraction peaks are well matched with the CoCrFeNiCu system of the reference card (ICDD:04-022-2302). Besides the phase identification, the XRD analysis can give information about the crystallinity of the cladded layers. The sharp and intense FCC diffraction peaks are obtained from the CoCrFeNi alloy and CoCrFeNiCu HEA cladded layers. The results indicate that the cladded layers are highly crystalline with well developed crystal structures, which is consistent with previous reports [38], [39].

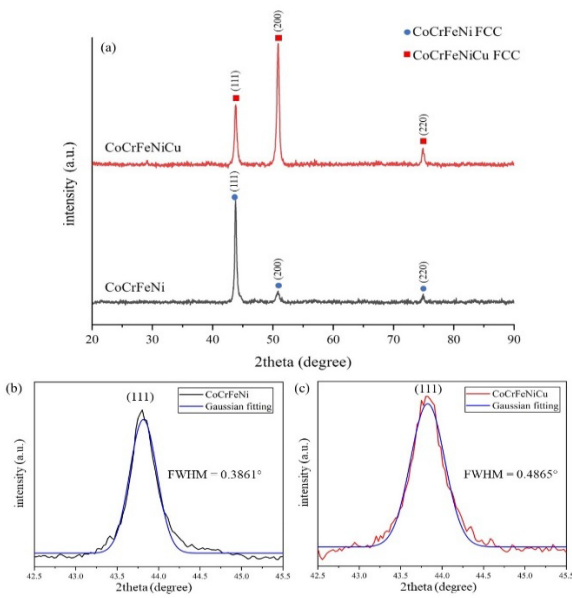

Figure 6: XRD patterns of (a) CoCrFeNi alloy and CoCrFeNiCu HEA cladded layers, (b) enlarged view of FCC (111) diffraction peak with Gaussian peak fitting of CoCrFeNi alloy and (c) CoCrFeNiCu HEA cladded layer.

Applied Science and Engineering Progress, Vol. 20, No. 3, 2027, 8288

The heat input by the GTAW process is sufficient to fully melt the alloy and solidify rapidly at the time of deposition. This leads to a well developed crystalline structure [17], [40].

It is noteworthy that no separate diffraction peaks are observed in the cladded layer of CoCrFeNiCu HEA (Figure 6(c)). However, the diffraction peak at 51.07° (200) has a higher intensity than the CoCrFeNi alloy cladded layer. As this behavior is observed, the Cu addition in the CoCrFeNiCu system causes a change in phase composition and lattice characteristics. Similar overlapping FCC diffraction peaks associated with Cu segregation have been reported in previous studies and can be explained by structural similarity and similar lattice parameters between the phases [25].

The previous study indicates that separate diffraction peaks related to Cu segregation may not always be identified, even if there is Cu segregation in the microstructure (Figure 3(d)). The lattice parameters of the Cu rich FCC phase are similar to the primary FCC matrix, and both phases may coexist, leading to overlapping diffraction peaks rather than distinct diffraction peaks [41].

Based on these results, the lattice characteristics and phase composition are similar to the main FCC matrix, although minor Cu segregation is observed. Therefore, the XRD pattern shows the dominant FCC structure, while the Cu segregation does not contribute to the separated diffraction peaks. The phase composition determined through this characterization is also consistent with the phase prediction from HEA design parameters (Table 2). It is predicted that the formation of the FCC solid solution phase happens when the ΔH_{mix} is within the range of -11.6 to 3.2 kJ/mol, δ is less than 6.6%, and VEC is ≥ 8 [27], [28]. These parameters are in the range mentioned above for both the CoCrFeNi alloy and the CoCrFeNiCu HEA cladded layers, which is also in good agreement with the XRD patterns. The enlarged views of the FCC (111) diffraction peak with Gaussian peak fitting for the CoCrFeNi alloy and CoCrFeNiCu HEA cladded layers are shown in Figure 6(b) and (c). Based on the results of the Gaussian fitting, the CoCrFeNiCu HEA cladded layer has a broader diffraction peak with a larger full width half maximum (FWHM) value of 0.4865° compared with the CoCrFeNi alloy cladded layer (0.3861°). The increase in FWHM suggests an increase in lattice strain and an increase in the density of crystal defects that are introduced during solidification [42]. The broadening of diffraction peaks due to these crystal defects is expected to enhance the hardness of the CoCrFeNiCu HEA cladded layer caused by the combined effect of lattice distortion and dislocation strengthening [7].

The calculated lattice parameters from the diffraction peaks of the FCC are shown in Table 4. The lattice parameter increased from 3.5646 Å to 3.5727 Å for the CoCrFeNi alloy and the CoCrFeNiCu HEA cladded layer, respectively. The slight increase in the lattice can be attributed to the substitution of Cu atoms in the FCC lattice, as Cu has a larger atomic radius than Co, Cr, Fe, and Ni. However, the difference was relatively small. This result is consistent with the possibility that the FCC diffraction peaks of the primary matrix and Cu segregation may overlap each other and prevent the formation of distinct Cu rich diffraction peaks [25].

Table 4: Calculated lattice parameters of the CoCrFeNi alloy and CoCrFeNiCu HEA cladded layers obtained from diffraction peaks.

Alloy	Peak	2θ (°)	d-spacing (Å)	Lattice parameter (Å)	Reference code
CoCrFeNi	111	43.96	2.0581	a=b=c =3.5646	ICDD: 04-018-7506
	200	51.21	1.7824		
	220	75.36	1.2602		
CoCrFeNiCu	111	43.89	2.0612	a=b=c =3.5727	ICDD: 04-022-2302
	200	51.07	1.7870		
	220	75.12	1.2636		

3.4 *Hardness*

Figure 7 presents the average Vickers hardness (mean ± standard deviation (SD)) of the cladded layer, HAZ, and substrate for the CoCrFeNi alloy and CoCrFeNiCu HEA systems. Statistical significance was evaluated using analysis of variance (ANOVA) followed by Fisher's least significant difference (LSD) post hoc test. Table 5 presents the individual Vickers hardness values together with the corresponding average hardness (mean ± SD) from ten measurements obtained at the designated indentation positions in each region illustrated in Figure 2. For the CoCrFeNi alloy system, the cladded layer exhibited the lowest hardness of 126.6 ± 2.8 HV, whereas the substrate and HAZ had hardness values of 147.4 ± 4.0 HV and 150.0 ± 3.0 HV, respectively. The lower hardness of the CoCrFeNi alloy cladded layer is due to the formation of a single FCC phase and homogeneous microstructure, as confirmed by the XRD results

(Figure 6) and SEM observations (Figure 3(c) and 4(a)). In contrast, the CoCrFeNiCu system exhibits a different hardness distribution. The cladded layer shows the highest hardness of 163.9 ± 2.2 HV, while the substrate and HAZ exhibit hardness values of 145.9 ± 2.9 HV and 151.5 ± 1.6 HV, respectively. The CoCrFeNiCu HEA cladded layer consistently exhibits higher hardness than the CoCrFeNi alloy cladded layer. Statistical analysis confirmed that the hardness of the CoCrFeNiCu HEA cladded layer is significantly higher than that of the CoCrFeNi alloy cladded layer (p-value < 0.001). However, the hardness differences between the two alloy systems in the HAZ (p-value = 0.1737) and substrate (p-value = 0.3237) are not statistically significant. The enhanced hardness is mainly attributed to elemental segregation during solidification with Cu addition, which leads to compositional heterogeneity (Figure 3(d) and 4(b)) [9], [43]. This compositional heterogeneity results in lattice distortion strengthening, which is consistent with the increase in lattice parameter and broader FWHM in the XRD analysis (Figure 6), indicating the increased lattice strain due to Cu addition [7]. Other alloy systems have also reported similar strengthening mechanisms associated with the resistance of dislocation motion caused by alloying elements [43], [44].

The hardness distribution of the cladded layer, HAZ, and substrate indicates the thermal gradient and microstructural evolution during the GTAW cladding process. A slight increase in the HAZ hardness with respect to the substrate can be interpreted as the effect of the heat-induced microstructural refinement during the thermal cycle of the welding. Overall, the results indicate that the hardness of the CoCrFeNi alloy cladded layer can be efficiently improved by Cu addition in the CoCrFeNiCu HEA cladded layer due to the combined effects of elemental segregation, lattice distortion, and microstructural evolution. These results suggest that the introduction of Cu can be an effective way to improve the mechanical properties of CoCrFeNi-based HEA cladded layers for surface engineering applications [45].

3.5 *Corrosion behavior*

Figure 8 shows the SEM images of the corroded surface and corresponding EDS mappings of the CoCrFeNi alloy and CoCrFeNiCu HEA cladded layers after electrochemical corrosion analysis. The

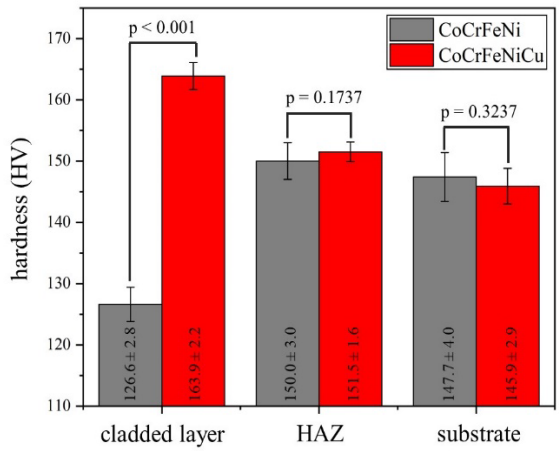

Figure 7: Average Vickers hardness of cladded layer, HAZ, and substrate of CoCrFeNi alloy and CoCrFeNiCu HEA systems.

Table 5: Individual Vickers hardness measurements and average hardness of cladded layer, HAZ, and substrate of CoCrFeNi alloy and CoCrFeNiCu HEA systems.

CoCrFeNi	**Hardness (HV)**		
Position	**Cladded layer**	**HAZ**	**Substrate**
1	126.4	150.9	147.8
2	129.8	144.8	148.7
3	124.2	148.1	153.2
4	130.2	153.4	141.4
5	131.1	149.4	148.4
6	125.5	149.5	143.3
7	123.1	153.8	143.6
8	126.5	146.4	148.2
9	124.2	153.4	146.1
10	124.5	149.8	153.6
Average hardness	126.6 ± 2.8	150.0 ± 3.0	147.4 ± 4.0
CoCrFeNiCu	**Hardness (HV)**		
Position	**Cladded layer**	**HAZ**	**Substrate**
1	166.7	151.6	145.7
2	163.9	148.7	145.6
3	165.9	149.9	144.4
4	163.4	151.4	144.8
5	159.4	152.1	145.7
6	162.7	154.0	141.7
7	166.3	150.1	142.3
8	163.6	152.7	149.0
9	164.9	152.9	150.6
10	161.7	151.4	148.7
Average hardness	163.9 ± 2.2	151.5 ± 1.6	145.9 ± 2.9

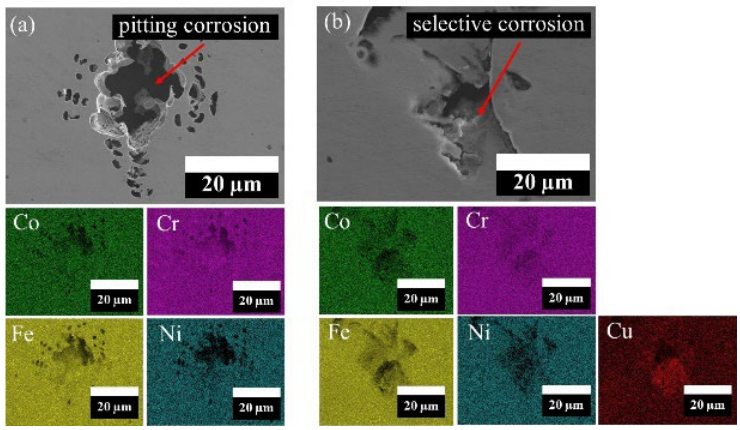

Figure 8: SEM images and corresponding EDS mappings of the corroded surface of (a) CoCrFeNi alloy and (b) CoCrFeNiCu HEA cladded layers.

corroded surface of the cladded layer of CoCrFeNi alloy (Figure 8(a)) shows pitting corrosion with localized cavities and deep pits. The formation of these pits is evidence of localized breakdown of the passive oxide film under chloride-containing conditions. After the passive film is broken, aggressive Cl^- ions penetrate the exposed surface and promote the pit initiation, followed by the localized dissolution and continuous pit propagation [46], [47].

In contrast, the CoCrFeNiCu HEA cladded layer (Figure 8(b)) shows selective corrosion instead of pitting corrosion. Corrosion preferentially occurs adjacent to the Cu segregation rather than deep pits. The corresponding EDS mappings show that these regions correspond to Cu segregation formed during solidification. The compositional heterogeneity between the Cu segregation and the surrounding CoCrFeNi matrix (Figure 5(b)) results in electrochemical differences and promotes microgalvanic coupling in the chloride-containing electrolyte. Consequently, the adjacent matrix becomes more susceptible to corrosion, resulting in selective corrosion instead of pitting corrosion [48].

The linear polarization curves for the CoCrFeNi alloy and CoCrFeNiCu HEA cladded layers in 3.5 wt% NaCl solution are presented in Figure 9, and the corresponding corrosion parameters are summarized in Table 6. Corrosion potential (E_{corr}) reflects the thermodynamic tendency for corrosion, whereas corrosion current density (i_{corr}) indicates the corrosion kinetics. The CoCrFeNi alloy cladded layer presents a lower i_{corr} of 6.92 µA/cm^2 and a higher E_{corr} of -492 mV vs. SCE compared to the CoCrFeNiCu HEA cladded layer (19.50 µA/cm^2 and -621 mV vs. SCE, respectively). The obtained electrochemical corrosion parameters suggest that the CoCrFeNi alloy cladded layer exhibits superior corrosion resistance [49]. In addition, the pitting potential (E_{pitt}) of the CoCrFeNi alloy cladded layer is 427 mV vs. SCE and the passive region (ΔE_{pass}) is 919 mV vs. SCE, which are higher than the values of 79 mV vs. SCE and 700 mV vs. SCE for the CoCrFeNiCu HEA cladded layer. The results indicate that the passive film formed on the CoCrFeNi alloy cladded layer is more stable and more resistant to passive film breakdown. The formation of a stable Cr-rich passive oxide film effectively inhibits the penetration of Cl^- ions, which results in the improved passivation of the CoCrFeNi alloy cladded layer [46], [47].

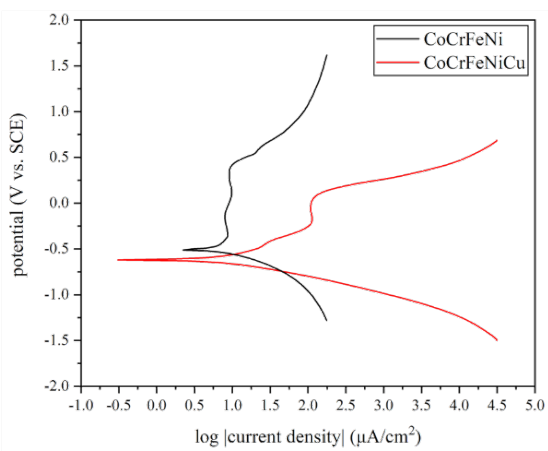

Figure 9: Linear polarization curve of CoCrFeNi alloy and CoCrFeNiCu HEA cladded layers in 3.5 wt% NaCl solution.

In contrast, the heterogeneous microstructure in the CoCrFeNiCu HEA cladded layer disrupts the formation of a uniform passive oxide film. The Cu segregation and the surrounding matrix establish microgalvanic coupling, which weakens the passive oxide film. This facilitates Cl^- ion penetration and consequently reduces the passivation of the CoCrFeNiCu HEA cladded layer [48].

Table 6: Electrochemical corrosion parameters of CoCrFeNi alloy and CoCrFeNiCu HEA cladded layers in 3.5 wt% NaCl solution.

Alloys	i_{corr} ($\mu A/cm^2$)	E_{corr} (mV vs. SCE)	E_{pitt} (mV vs. SCE)	ΔE_{pass} (mV vs. SCE)
CoCrFeNi	6.92	-492	427	919
CoCrFeNiCu	19.50	-621	79	700

Figure 10 shows the electrochemical impedance spectra of the CoCrFeNi alloy and CoCrFeNiCu HEA cladded layers, and Table 7 presents the corresponding electrochemical impedance parameters calculated from an equivalent electrical circuit (EEC) fitting. The single capacitive loop found in the Nyquist plots of both cladded layers (Figure 10(a) and (b)) indicates that the electrochemical response is mainly controlled by the reactions through the passive surface film. This is in agreement with the interpretation of electrochemical impedance spectra reported in previous studies [22], [50].

The $R_s{\cdot}[R_{oxide}CPE_{oxide}]$ EEC used to fit the impedance spectra is shown in Figure 10(e). The EEC consists of the solution resistance (R_s), oxide film resistance (R_{oxide}) and a constant phase element (CPE_{oxide}) [17]. The intercept of the Nyquist semicircle with the Z' axis at high frequency represents the R_s. The second intercept at low frequency corresponds to the total resistance (R_s+R_{oxide}). Since the low frequency intercept cannot be determined directly from the experimental curve, it was obtained by fitting the impedance data using the EEC. Therefore, the difference between the two intercepts represents the oxide film resistance (R_{oxide}). A larger semicircle diameter demonstrates a higher oxide film resistance. The CoCrFeNi alloy cladded layer has a larger semicircle diameter than that of the CoCrFeNiCu HEA cladded layer, indicating higher electrochemical stability and corrosion resistance.

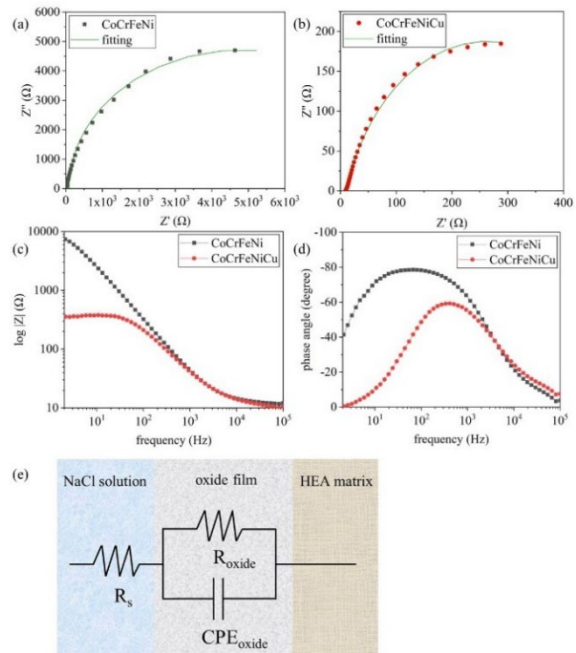

Figure 10: Electrochemical impedance spectroscopy results in 3.5 wt% NaCl solution: (a) Nyquist plot of CoCrFeNi alloy cladded layer, (b) Nyquist plot of CoCrFeNiCu HEA cladded layer, (c) Bode impedance plots, (d) Bode phase plots, and (e) the equivalent electrical circuit used for impedance fitting.

Furthermore, an increase in the imaginary impedance (Z'') at medium frequencies confirms the capacitive behavior of the passivating oxide layer [51]. The Bode impedance plots (Figure 10(c)) further confirm the Nyquist analysis. The CoCrFeNi alloy cladded layer has higher impedance in a low frequency region, indicating a higher resistance of the oxide film (R_{oxide}) and a more protective passive film than the CoCrFeNiCu HEA cladded layer.

Table 7: Electrochemical impedance parameters obtained from equivalent electrical circuit fitting of CoCrFeNi alloy and CoCrFeNiCu HEA cladded layers.

Alloys	R_s ($\Omega{\cdot}cm^2$)	R_{oxide} ($k\Omega{\cdot}cm^2$)	CPE_{oxide} ($\mu F{\cdot}cm^{-1}s^{\alpha-1}$)	n	Chi-sqr	Sum-sqr
CoCrFeNi	12.32	12.48	92.02	0.90	0.0014	0.0301
CoCrFeNiCu	10.77	0.51	21.53	0.81	0.0012	0.0736

Applied Science and Engineering Progress, Vol. 20, No. 3, 2027, 8288

The EIS results provide further insight into the corrosion mechanisms based on the SEM images and EDS mapping (Figure 8). The CoCrFeNi alloy cladded layer has a higher R_{oxide} (12.48 $k\Omega \cdot cm^2$) than the CoCrFeNiCu HEA cladded layer (0.51 $k\Omega \cdot cm^2$), indicating the formation of a more protective and stable passive oxide film [52]. This result is in agreement with the homogeneous elemental distribution of the CoCrFeNi alloy cladded layer observed by EDS mapping in Figure 8(a). The uniform elemental distribution promotes the formation of a continuous and stable passive oxide film. The breakdown of the passive film is localized and leads to pitting corrosion. However, the CoCrFeNiCu HEA cladded layer presents a lower R_{oxide} value, indicating the formation of a less continuous and less protective passive oxide film. EDS mapping (Figure 8(b)) revealed a significant segregation of Cu in the cladded layer, which led to compositional heterogeneity between Cu segregation and the surrounding CoCrFeNi matrix. These electrochemical potential differences promote microgalvanic coupling, resulting in dissolution of the adjacent matrix and degradation of passive film integrity. The results suggest that the passive film becomes less uniform and less protective, leading to the selective corrosion observed in Figure 8(b) [53].

The Bode phase plots (Figure 10(d)) further support the proposed corrosion mechanisms. The CoCrFeNi alloy cladded layer exhibits a larger maximum phase angle (-78°) and a higher CPE_{oxide} (92.02 $\mu F \cdot cm^{-1}s^{\alpha-1}$) than the CoCrFeNiCu HEA cladded layer (-59° and 21.53 $\mu F \cdot cm^{-1}s^{\alpha-1}$, respectively). These results suggest the formation of a more homogeneous passive oxide film with better capacitive properties [54]. This interpretation is consistent with pitting corrosion as shown in Figure 8(a), where corrosion occurs only after passive film breakdown. However, the lower phase angle and R_{oxide} value of the CoCrFeNiCu HEA cladded layer show a less stable passive film due to the heterogeneous microstructure. The compositional heterogeneity due to Cu segregation is confirmed by the EDS mappings (Figure 8(b)). Overall, the EIS results are in good agreement with the EDS mapping and the observed corrosion behavior. These observations suggest that Cu segregation disrupts passive film stability and promotes selective corrosion through microgalvanic effects [48].

4 Conclusions

In the present work, equiatomic CoCrFeNi alloy and CoCrFeNiCu HEA cladded layers have been successfully fabricated on SS304 substrates using the GTAW cladding process. The main findings according to the results of the experimental investigation are summarized as follows. The CoCrFeNi alloy and CoCrFeNiCu HEA cladded layers revealed a single FCC phase with strong metallurgical bonding to the SS304 substrate. The CoCrFeNi alloy cladded layer had a homogeneous microstructure, while the CoCrFeNiCu HEA cladded layer exhibited compositional heterogeneity with Cu segregation due to the positive ΔH_{mix} between Cu and the other constituent elements. Cu addition increased the CoCrFeNi alloy cladded layer hardness from 126.6 ± 2.8 HV to 163.9 ± 2.2 HV. The increased hardness was attributed to the heterogeneous microstructure and the lattice distortion strengthening caused by Cu addition. The CoCrFeNi alloy cladded layer exhibited superior corrosion resistance in 3.5 wt% NaCl solution compared to the CoCrFeNiCu HEA cladded layer with lower i_{corr} (6.92 $\mu A/cm^2$), higher E_{corr} (-492 mV vs. SCE), wider passive region (919 mV vs. SCE), and higher oxide film resistance (12.48 $k\Omega \cdot cm^2$). The improved corrosion resistance was attributed to the formation of a more stable passive oxide film, but the Cu segregation caused compositional heterogeneity, which resulted in a less uniform passive film and selective corrosion through microgalvanic coupling. Cu addition affected the microstructure, hardness, and corrosion behavior of the CoCrFeNi HEA cladded layer, in which a tradeoff between hardness and corrosion resistance was observed. These results highlight the importance of compositional design for the tailoring of the properties of HEA cladded layers for advanced surface engineering applications.

Acknowledgments

This research project is supported by National Research Council of Thailand (NRCT): (Contact No. N41A650071). In addition, the support provided by Kasetsart University, particularly the Faculty of Engineering, Kasetsart University Research and Development Institute (KURDI), Thailand is acknowledged.

Author Contributions

P.C.: research design, conceptualization, investigation, writing an original draft, reviewing and editing; T.S.: data curation; S.P.: data curation; A.R.: conceptualization, data curation, writing-reviewing and editing, project administration. All authors have read and agreed to the published version of the manuscript.

Conflicts of Interest

The authors declare no conflict of interest.

Declaration of generative AI and AI-assisted technologies in the writing process

The authors utilized the ChatGPT tool to enhance the language and readability of the manuscript.

References

[1] J. W. Yeh, Y. L. Chen, S. J. Lin, and S. K. Chen, "High-entropy alloys – a new era of exploitation," *Materials Science Forum*, vol. 560, pp. 1–9, Nov. 2007, doi: 10.4028/www.scientific.net/MSF.560.1.

[2] B. Cantor, I. T. H. Chang, P. Knight, and A. J. B. Vincent, "Microstructural development in equiatomic multicomponent alloys," *Materials Science and Engineering: A*, vol. 375–377, pp. 213-218, Jul. 2004, doi: 10.1016/j.msea.2003.10.257.

[3] T. Sonar, M. Ivanov, E. Trofimov, A. Tingaev, and I. Suleymanova, "An overview of microstructure, mechanical properties and processing of high entropy alloys and its future perspectives in aeroengine applications," *Materials Science for Energy Technologies*, vol. 7, pp. 35-60, Jul. 2023, doi: 10.1016/ j.mset.2023.07.004.

[4] M. Vaidya, K. Guruvidyathri, and B. S. Murty, "Phase formation and thermal stability of CoCrFeNi and CoCrFeMnNi equiatomic high entropy alloys," *Journal of Alloys and Compounds*, vol. 774, pp. 856-864, Feb. 2019, doi: 10.1016/j.jallcom.2018.09.342.

[5] P. Muangtong, A. Rodchanarowan, D. Chaysuwan, N. Chanlek, and R. Goodall, "The corrosion behaviour of CoCrFeNi-x (x = Cu, Al, Sn) high entropy alloy systems in chloride solution," *Corrosion Science*, vol. 172, Art. no. 108740, Aug. 2020, doi: 10.1016/j.corsci.2020.108740.

[6] A. C. Fan, J. H. Li, and M. H. Tsai, " On the phase constituents of three CoCrFeNiX (X = V, Nb, Ta) high-entropy alloys after prolonged annealing," *Journal of Alloys and Compounds*, vol. 823, Art. no. 153524, May 2020, doi: 10.1016/j.jallcom.2019.153524.

[7] X. Wang et al., "Microstructural evolution and mechanical properties of novel nanoparticles strengthened CoCrFeNi based high entropy alloy," *Journal of Materials Research and Technology*, vol. 25, pp. 7325-7334, Sep. 2023, doi: 10.1016/j.jmrt.2023.07.070.

[8] W. L. Wang and Z. H. Kong, "Phase separation and microhardness of rapidly solidified high-entropy CoCrFeNiCux alloys," *Journal of Alloys and Compounds*, vol. 853, Art. no. 156451, Feb. 2021, doi: 10.1016/j.jallcom.2020.156451.

[9] H. Zheng et al., "Microstructure evolution, Cu segregation and tensile properties of CoCrFeNiCu high entropy alloy during directional solidification," *Journal of Materials Science & Technology*, vol. 38, pp. 19-27, Feb. 2020, doi: 10.1016/j.jmst.2019.08.019.

[10] Q. Hu, H. L. Wang, L. H. Qian, L. C. Zeng, Q. Wang, and X. W. Liu, "Effects of Cu additions on microstructure and mechanical properties of as-cast $CrFeCoNiCu_x$ high-entropy alloy," *Transactions of Nonferrous Metals Society of China*, vol. 33, no. 6, pp. 1803-1813, Jun. 2023, doi: 10.1016/S1003-6326(23)66223-5.

[11] J. P. Davim, Ed., *Welding Technology* (Materials Forming, Machining and Tribology). Cham, Switzerland: Springer, 2021. doi: 10.1007/978-3-030-63986-0.

[12] Y. Liu, Y. Ding, L. Yang, R. Sun, T. Zhang, and X. Yang, "Research and progress of laser cladding on engineering alloys: A review," *Journal of Manufacturing Processes*, vol. 66, pp. 341-363, Jun. 2021, doi: 10.1016/j.jmapro.2021.03.061.

[13] D. Wu, Y. Yang, J. Cheng, and X. Li, "Improving the wear and corrosion properties of plasma clad CoCrFeMnNi high entropy alloy coating by low-temperature plasma nitriding," *Surface and Coatings Technology*, vol. 520, Art. no. 133080, Jan. 2026, doi: 10.1016/j.surfcoat.2025.133080.

[14] Y. Bai et al., "Phase transition and heterogeneous strengthening mechanism in CoCrFeNiMn high-entropy alloy fabricated by laser-engineered net shaping via annealing at intermediate-temperature," *Journal of Materials Science & Technology*, vol. 92,

pp. 129–137, Dec. 2021, doi: 10.1016/j.jmst.2021.03.028.

[15] K. Ananthakumar, D. Rajamani, E. Balasubramanian, and J. P. Davim, "Measurement and optimization of multi-response characteristics in plasma arc cutting of Monel 400™ using RSM and TOPSIS," *Measurement*, vol. 135, pp. 725-737, Mar. 2019, doi: 10.1016/j.measurement.2018.11.076.

[16] J. P. Davim, C. Oliveira, and A. Cardoso, "Predicting the geometric form of clad in laser cladding by powder using multiple regression analysis (MRA)," *Materials & Design*, vol. 29, no. 2, pp. 554-557, Dec. 2008, doi: 10.1016/j.matdes.2007.01.023.

[17] S. Jaturapronperm et al., "The effect of Sn and Ti addition in CoCrFeNi to prepare equiatomic high entropy alloy cladded on 304 stainless steels via gas tungsten arc cladding," *Materials Characterization*, vol. 224, Art. no. 115048, Jun. 2025, doi: 10.1016/j.matchar.2025.115048.

[18] Q. Fan et al., "Effect of high Fe content on the microstructure, mechanical and corrosion properties of AlCoCrFeNi high-entropy alloy coatings prepared by gas tungsten arc cladding," *Surface and Coatings Technology*, vol. 418, Art. no. 127242, Jul. 2021, doi: 10.1016/j.surfcoat.2021.127242.

[19] Y. C. Lin and Y. Y. Liu, "Effects of Co and W on the microstructure and wear behavior of NiCrAlMoTiFeNbX equimolar multicomponent-clad layers," *Wear*, vols. 446–447, Art. no. 203186, Apr. 2020, doi: 10.1016/j.wear.2020.203186.

[20] Q. Fan et al., "AlCoCrFeNi high-entropy alloy coatings prepared by gas tungsten arc cladding: Microstructure, mechanical and corrosion properties," *Intermetallics*, vol. 138, Art. no. 107337, Nov. 2021, doi: 10.1016/j.intermet.2021.107337.

[21] J. P. Davim, "Welding: A bibliometric analysis," *International Journal of Materials Engineering Innovation*, vol. 16, no. 2, pp. 111–113, May 2025.

[22] C. Zheng, Z. Liu, Q. Liu, Y. Kong, S. Guo, and C. Liu, "Electrochemical behavior and passive film properties of Hastelloy C22 alloy, laser-cladding C22 coating, and Ti–6Al–4V alloy in sulfuric acid dew-point corrosion environment," *Metals*, vol. 12, no. 4, Art. no. 683, Apr. 2022, doi: 10.3390/met12040683.

[23] L. Sun et al., "Microstructure, mechanical and corrosion properties of $(CoCrFeNi)_{82-x}(NiAl)_{18}Nb_x$ triple-phase high-entropy alloys," *Materials Science and Engineering: A,* vol. 948, Art. no. 149301, Nov. 2025, doi: 10.1016/j.msea.2025.149301.

[24] Y. Zhang, X. Chen, S. Jayalakshmi, R. A. Singh, V. B. Deev, and E. S. Prusov, "Factors determining solid solution phase formation and stability in $CoCrFeNiX_{0.4}$ (X = Al, Nb, Ta) high entropy alloys fabricated by powder plasma arc additive manufacturing," *Journal of Alloys and Compounds*, vol. 857, Art. no. 157625, Mar. 2021, doi: 10.1016/j.jallcom.2020.157625.

[25] A. Takeuchi and A. Inoue, "Classification of bulk metallic glasses by atomic size difference, heat of mixing and period of constituent elements and its application to characterization of the main alloying element," *Materials Transactions*, vol. 46, no. 12, pp. 2817–2829, Dec. 2005, doi: 10.2320/matertrans.46.2817.

[26] S. Guo and C. T. Liu, "Phase stability in high entropy alloys: Formation of solid-solution phase or amorphous phase," *Progress in Natural Science: Materials International*, vol. 21, no. 6, pp. 433–446, Dec. 2011, doi: 10.1016/S1002-0071(12)60080-X.

[27] S. Guo, C. Ng, J. Lu, and C. T. Liu, "Effect of valence electron concentration on stability of fcc or bcc phase in high entropy alloys," *Journal of Applied Physics*, vol. 109, no. 10, Art. no. 103505, May 2011, doi: 10.1063/1.3587228.

[28] S. Guo, Q. Hu, C. Ng, and C. T. Liu, "More than entropy in high-entropy alloys: Forming solid solutions or amorphous phase," *Intermetallics*, vol. 41, pp. 96-103, Oct. 2013, doi: 10.1016/j.intermet.2013.05.002.

[29] D. J. M. King, S. C. Middleburgh, A. G. McGregor, and M. B. Cortie, "Predicting the formation and stability of single phase high-entropy alloys," *Acta Materialia*, vol. 104, pp. 172–179, Feb. 2016, doi: 10.1016/j.actamat.2015.11.040.

[30] S. Pathompakawant, P. Kowitwarangkul, P. Ninpetch, and S. Otarawanna, "Effects of pulsed laser repetition rate and duty cycle on heat-affected zone narrowing in laser powder bed fusion of 316L stainless steel," *Applied Science and Engineering Progress*, vol. 18, no. 4, Art. no. 7709, Oct. 2025, doi: 10.14416/j.asep.2025.03.007.

[31] A. Khajuria et al., "Influence of boron on microstructure and mechanical properties of Gleeble simulated heat-affected zone in P91 steel," *International Journal of Pressure Vessels and Piping*, vol. 188, Art. no. 104246, doi: 10.1016/j.ijpvp.2020.104246.

[32] M. Akhtar, A. Khajuria, V. Kumar, R. K. Gupta, and S. K. Albert, "Evolution of microstructure during welding simulation of boron modified P91 steel,"

Physics of Metals and Metallography, vol. 120, no. 7, pp. 672–685, Jul. 2019, doi: 10.1134/S0031918X19070056.

[33] A. Khajuria, M. Akhtar, and R. Bedi, "Boron addition to AISI A213/P91 steel: Preliminary investigation on microstructural evolution and microhardness at simulated heat-affected zone," *Materials Science and Engineering Technology*, vol. 53, no. 10, pp. 1167-1183, Oct. 2022, doi: 10.1002/mawe.202100152.

[34] A. Azwinur, M. H. Kusuma, U. Usman, S. Dharma, and A. Akhyar, "Effects of heat input on mechanical properties, microstructures and thermal conductivity of copper alloy in gas tungsten arc welding technology," *Advances in Science and Technology Research Journal*, vol. 19, no. 6, pp. 316-329, 2025, doi: 10.12913/22998624/203367.

[35] H. Schwarz et al., "Fabrication of single-crystalline CoCrFeNi thin films by DC magnetron sputtering: A route to surface studies of high-entropy alloys," *Advanced Materials*, vol. 35, no. 36, Art. no. 2301526, Sep. 2023, doi: 10.1002/adma.202301526.

[36] S. Mukanov, P. Loginov, A. Fedotov, M. Bychkova, M. N. Fatykhova, and E. Levashov, "The effect of copper on the microstructure, wear and corrosion resistance of CoCrCuFeNi high-entropy alloys manufactured by powder metallurgy," *Materials*, vol. 16, no. 3, Art. no. 1178, Jan. 2023, doi: 10.3390/ma16031178.

[37] Y. Wang et al., "Effect of Cu content on the tribological behavior of CuxCoCrMoNi high-entropy alloys," *Journal of Materials Research and Technology*, vol. 36, pp. 6982–6993, May–Jun. 2025, doi: 10.1016/j.jmrt.2025.04.292.

[38] B. Saha, A. Sathyan, P. Singh, A. S. Kalamdhad, and M. Khwairakpam, "Prerequisite of electrohydrolysis pretreatment on lignocellulose terrestrial weed (*Ageratum conyzoides*) to enhance the methane production and continuous reactor study," *Materials Science for Energy Technologies*, vol. 3, pp. 896-904, 2020, doi: 10.1016/j.mset.2020.10.006.

[39] B. Saha, A. S. Kalamdhad, and M. Khwairakpam, "Efficiency of electrohydrolysis pretreatment on terrestrial weed (*Parthenium hysterophorus*) to cut down the hydrolysis stage during the anaerobic digestion process and continuous reactor study," *Energy Reports*, vol. 7, pp. 3547-3555, Nov. 2021, doi: 10.1016/j.egyr.2021.06.023.

[40] E. J. da Cruz Junior et al., "Impact of heat input on the cladding of super austenitic stainless steel through the gas tungsten arc welding process on ASTM A516 Grade 70 steel," *Coatings*, vol. 14, no. 11, Art. no. 1356, Nov. 2024, doi: 10.3390/coatings14111356.

[41] A. Verma et al., "High temperature wear in $CoCrFeNiCu_x$ high entropy alloys: The role of Cu," *Scripta Materialia*, vol. 161, pp. 28–31, Mar. 2019, doi: 10.1016/j.scriptamat.2018.10.007.

[42] M. Akhtar et al., "Phase transformations and numerical modelling in simulated HAZ of nanostructured P91B steel for high temperature applications," *Applied Nanoscience*, vol. 8, no. 7, pp. 1669–1685, Oct. 2018, doi: 10.1007/s13204-018-0854-1.

[43] C. M. Yang et al., "Effect of Cu-doping on tribological properties of laser-cladded $FeCoCrNiCu_x$ high-entropy alloy coatings," *Tribology International*, vol. 188, Art. no. 108868, Oct. 2023, doi: 10.1016/j.triboint.2023.108868.

[44] N. Hanumantharayappa, P. Sanikere, R. Kodandappa, and S. Nagaraja, "Mechanical characterization of Cu-Al-based shape memory alloys: Influence of Mn, Be and Fe on tensile strength, yield stress, yield strain, ductility and hardness," *Applied Science and Engineering Progress*, vol. 19, no. 2, Art. no. 7981, Apr. 2026, doi: 10.14416/j.asep.2025.11.006.

[45] V. Burgio and G. Moeini, "Laser powder bed fusion additive manufacturing of a CoCrFeNiCu high-entropy alloy: Processability, microstructural insights, and (in situ) mechanical behavior," *Materials*, vol. 18, no. 13, Art. no. 3071, Jul. 2025, doi: 10.3390/ma18133071.

[46] J. Recio-Hernandez, M. Galicia-García, H. Silva-Jiménez, R. Malpica-Calderón, and E. G. Ordoñez-Casanova, "EIS evaluation of corrosion resistance of AISI 304 stainless steel exposed to *Pseudomonas stutzeri*," *International Journal of Electrochemical Science*, vol. 16, no. 5, Art. no. 21058, May 2021, doi: 10.20964/2021.05.39.

[47] K. Li et al., "Pitting corrosion of 304 stainless steel in secondary water supply system," *Corrosion Communications*, vol. 7, pp. 43–50, Sep. 2022, doi: 10.1016/j.corcom.2021.11.010.

[48] L. Du et al., "Inhomogeneous phases in Cu-Zn-Al-Fe-Mn and the micro-galvanic coupling in 3.5 wt% NaCl solutions at different pH," *Corrosion Science*, vol. 195, Art. no. 110005, Feb. 2022, doi: 10.1016/j.corsci.2021.110005.

[49] C. Eguico et al., "Sonophotopythochemical functionalization of graphene oxide–Al–Zn bimetal

nanocomposite for corrosion inhibition," *Applied Science and Engineering Progress*, ol. 18, no. 2, Art. no. 7613, Apr. 2025, doi: 10.14416/j.asep.2024. 10.004.

[50] U. Farahdina et al., "Electrochemical characterization of thin film/nanodots electrodes of silver and gold for biosensing CCRF-CEM leukemia cells," *Applied Science and Engineering Progress*, vol. 18, no. 1, Art. no. 7529, Jan. 2025, doi: 10.14416/j.asep.2024.09.003.

[51] P. Muangtong, R. M. Namus, and R. Goodall, "Improved tribocorrosion resistance by addition of Sn to CrFeCoNi high entropy alloy," *Metals*, vol. 11, no. 1, Art. no. 13, Dec. 2020, doi: 10.3390/met11010 013.

[52] J. Zhou, Y. Cheng, Y. Wan, H. Chen, Y. Wang, and J. Yang, "Strengthening by Ti, Nb, and Zr doping on microstructure, mechanical, tribological, and corrosion properties of CoCrFeNi high-entropy alloys," *Journal of Alloys and Compounds*, vol. 984, Art. no. 173819, May 2024, doi: 10.1016/j.jallcom. 2024.173819.

[53] X. Chen, H. Qian, Y. Lou, B. Yang, T. Cui, and D. Zhang, "Effects of Cu-content and passivation treatment on the corrosion resistance of $Al_{0.3}Cu_xCoCrFeNi$ high-entropy alloys," *Journal of Alloys and Compounds*, vol. 920, Art. no. 165956, Nov. 2022, doi: 10.1016/j.jallcom.2022.165956.

[54] B. Seo, H.-K. Park, H.-G. Kim, W.-R. Kim, and K. Park, "Corrosion behavior of additive manufactured CoCr parts polished with plasma electrolytic polishing," *Surface and Coatings Technology*, vol. 406, Art. no. 126640, Feb. 2021, doi: 10.1016/j.surfcoat.2020.1266.